J. Fluid Mech. (1995), *vol.* 305, *pp.* 47–75

Numerical simulation of coastal upwelling and interfacial instability of a rotating and stratified fluid

By YAN ZANG[1,2] AND ROBERT L. STREET[1]

[1] Environmental Fluid Mechanics Laboratory, Stanford University, CA 94305-4020, USA

[2] Quantum Corporation, 500 McCarthy Blvd, Milpitas, CA 95035, USA

(Received 8 October 1994 and in revised form 18 May 1995)

The evolution of the coastal upwelling and interfacial instability of a stratified and rotating fluid is studied numerically by using large-eddy simulation. Upwelling is generated near the sidewall of a rotating annulus by the shear at the top. The fluid initially consists of a stably stratified 'two-layer' structure with a narrow interface separating the two layers. The large-scale motion of the flow is simulated by solving the time-dependent non-hydrostatic incompressible Navier–Stokes and scalar transport equations while the small-scale motion is represented by a dynamic subgrid-scale model. The upwelling process contains both stable and unstable stratification. The vertical structure of upwelling consists of a persistent primary front, a trailing mixing zone on the shore side of the front, and a temporary secondary front which leads a top inversion layer. The longshore velocity profile has two maxima which occur at the edge of the sidewall boundary layer and at the density front. The upwelled density front is unstable to azimuthal perturbations and baroclinic waves develop and grow to large amplitude. Pairs of cyclonic and anticyclonic waves appear at the front which form 'jet-streams'. The secondary front is unstable to azimuthal perturbations. Its instability, and the associated drop of the top inversion layer, take the form of radial bands which subsequently break up into isolated patches and eventually sink. The computed values of various upwelling time and length scales are compared to and are in good agreement with past experimental data.

1. Introduction

Coastal upwelling is a geophysical phenomenon which occurs mostly from spring to summer near the eastern boundary of the oceans. The direction of the coastal wind in this time period is predominantly equatorward. As the surface water moves with the wind, it is driven in the offshore direction by the Coriolis force due to the Earth's rotation (figure 1) which results in offshore Ekman transport. The result is that return flow under the surface layer is lifted upward near the coast. When the coastal wind is strong enough, the seasonal thermocline is elevated and intersects with the ocean surface to form a surface density front and an anomaly of cold water along the coast.

Coastal upwelling has significant effects on the weather, fish supply, ecology, and transport of nutrient and pollutant materials near the coast (Ryther 1969; Roughgarden, Gines & Possingham 1988). A large amount of increasingly sophisticated data on coastal upwelling has been compiled from field observations (e.g. Smith, Mooers & Enfield 1971; Mooers, Collins & Smith 1976; Halpern 1976; Ikeda, Mysak & Emery 1984; Mooers & Robinson 1984; Huyer, Smith & Paluszkiewicz 1987;

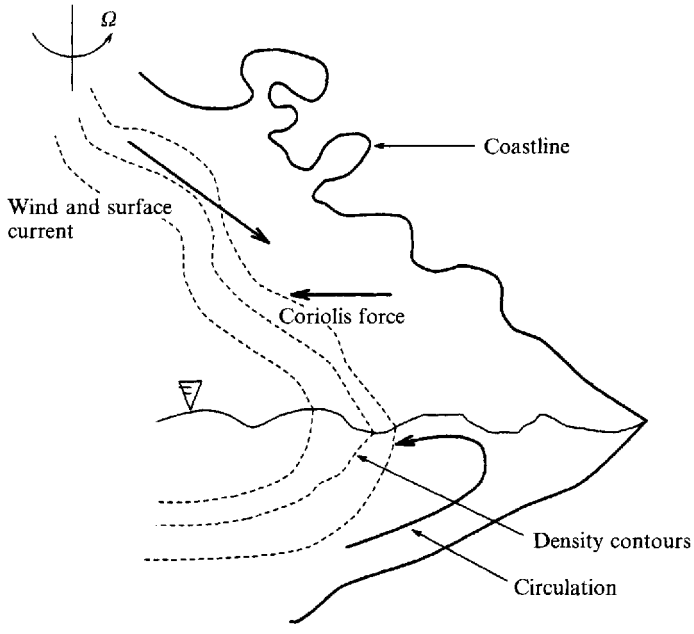

FIGURE 1. Schematic of coastal upwelling.

Petrie, Topliss & Wright 1987; Rienecker & Mooers 1987; Colin 1988). Among these, Rienecker & Mooers (1987) coupled their observations with an open-ocean quasi-geostrophic model to show that the model could provide useful dynamical interpolation between observation periods, yielding a time series of the evolution of features in a subdomain of the California current system. A survey of the coastal as well as open-sea upwelling research prior to 1967 can be found in Smith (1968). The main features of coastal upwelling include the following.

(i) The longshore flow in the surface layer which is in the direction of the wind has a jet-like structure and is largely in geostrophic balance.

(ii) There is a net offshore transport of water in the surface Ekman layer. The cross-stream circulation consists of two counterclockwisely rotating cells (when viewed against the wind direction). The dividing line of these two cells roughly corresponds to that which divides the surface layer from the opposing longshore undercurrent.

(iii) The frontal layer which intersects the surface remains largely stationary, even though the wind continues to be favourable to upwelling.

(iv) Both the horizontal and the vertical velocity gradients are high across the frontal layer. The frontal layer is also an internal turbulent shear layer where intensive mixing takes place.

(v) Waves, meanders and pinched-off eddies have been observed near the ocean surface front in the form of jets and cyclone/anticyclone pairs.

Laboratory experiments have been conducted to study coastal upwelling flow (e.g. Narimousa & Maxworthy 1985, 1987; Monismith 1986). Frontal waves and eddies have been observed in the laboratory experiments by many investigators (Hide 1971; Hart 1980; Linden & van Heijst 1984; Griffiths & Linden 1981, 1982; Narimousa & Maxworthy 1985, 1987). The experiments of Narimousa & Maxworthy will be given special attention because of the close resemblance of the geometry and flow conditions of our simulations to their experiments. Narimousa & Maxworthy conducted a series of laboratory experiments in which they set up a two-layer stratified system in a

rotating conical cylinder. The top disk was rotated opposite to the system rotation to simulate an upwelling-favourable surface wind stress. As a result, the density interface was elevated near the outer wall, and when the surface stress was strong enough, the interface intersected the surface and formed a front which continued to migrate offshore. The front was unstable under certain conditions and azimuthal waves appeared and grew to large amplitude. Using flow visualization, Narimousa & Maxworthy (1987, hereafter referred to as NM87) observed structures such as plumes, jets and pinched-off cyclones near the front.

Many models, analytical as well as numerical, have been proposed to describe certain aspects of coastal upwelling. Steady-state and homogeneous models were developed by, notably, Ekman (1905), Sverdrup (1938), Hidaka (1954) and Garvine (1971). The effect of stratification is considered either by the continuous approach or by the layered approach. Continuously stratified models were studied, for example, by Hsueh & Kenney (1972), Allen (1972*a*, *b*, 1973) and Pedlosky (1974). Two-layer stratified models were investigated analytically by Charney (1955) and Yoshida (1955, 1967). Yoshida (1955) considered the transient phases of coastal upwelling. His model has no variations in the longshore direction. For the upper layer, it assumes a geostrophic balance in the cross-shore direction and a balance among the transient advection, the Coriolis force and the surface wind stress in the longshore direction. An important result derived from this model is the surfacing time scale, t_f, of the interface which is

$$t_f = \rho h_{10} \mathscr{R} f / \tau_s, \tag{1}$$

where ρ is the fluid density, τ_s is the surface stress, $\mathscr{R}$ is the Rossby radius of deformation for the two-layer system defined as

$$\mathscr{R} = \frac{1}{f}\left[\frac{g' h_{10}(H - h_{10})}{H}\right]^{1/2}, \tag{2}$$

$H = h_{10} + h_{20}$ is the total depth of the water, h_{10} and h_{20} are, respectively, the initial depths of the upper and lower layers, f is the Coriolis parameter which is twice the angular velocity Ω of the Earth, and $g' = g\Delta\rho/\rho$ is the reduced gravity. The deformation radius $\mathscr{R}$ is the intrinsic horizontal length scale in a rotating two-layer system. Yoshida later extended this model to a two-layer quasi-steady-state model (Yoshida 1967).

Numerical models based on the layered approach were developed by O'Brien & Hurlburt (1972) and Hurlburt & Thompson (1973), were later extended to three dimensions by Peffley & O'Brien (1976) and were applied to study the effect of bottom topography by Preller & O'Brien (1980). The major advantage of a numerical model compared to the analytical models is its capability of dealing with nonlinearity and the complex geometry of the coast and the shelf. However, the continuous stratified model of Allen (1973) was restricted to laminar axisymmetric flow cases. On the other hand, until recently the main deficiency of the layered models is that they cannot be used to study the evolution of a surface front and associated cross-front turbulent mixing. Pelegri & Richman (1993) have presented a two-dimensional two-layer model for wind-driven transient coastal upwelling which allows mass and heat turbulent transfer between both layers.

More advanced primitive equation (hydrostatic pressure variation is assumed) codes are also being used now to study upwelling and related flows. Haidvogel, Beckman & Hedstrom (1991) and Song & Haidvogel (1994) provide excellent examples and show the value of fully three-dimensional simulations that can cover the flow region of interest. While Haidvogel *et al.* (1991) note that all of the important effects had not yet

been included in their model (e.g. wind stress), the model of Song & Haidvogel (1994) includes all of the key effects (e.g. variable topography, wind stress, free surface, turbulence, etc.).

The present work attempts a new approach to study coastal upwelling by using large-eddy simulation (LES). In LES, the grid-filtered time-dependent non-hydrostatic incompressible Navier–Stokes and scalar transport equations are solved and the small-scale motion is represented with a dynamic subgrid-scale model. By tracking the temporal evolution and resolving the spatial structure of the upwelling flow and the surface density front, we are able to 'see' various stages of the whole upwelling process and the interfacial instability from different angles. The main advantage of this approach over a hydrostatic model is that it includes all the dynamics in the simulation. The LES approach with dynamic subgrid-scale modelling allows accurate and robust representation of the small-scale motions by the resolved field which includes the effect of rotation and stratification. The disadvantage of LES is that it requires a large amount of computing resource as we can see in §4. In the present work, we intend to examine the efficacy of LES in the study of stratified and rotating flows in geometrically complex domains by comparing the simulation data with previous experimental and theoretical results and to provide new insight into the coastal upwelling process and interfacial instability.

This paper is organized as follows. In §2, the governing equations and the numerical methods are briefly described. Section 3 defines the computed upwelling flows which include the geometrical, physical and numerical parameters. A scaling analysis of the important length and time scales of the flow is carried out in §4. Section 5 contains the simulation results. Conclusions are given in §6.

2. Governing equations and numerical methods

The governing equations are the grid-filtered time-dependent three-dimensional incompressible Navier–Stokes, continuity, and scalar transport equations under the Boussinesq approximation. They are

$$\frac{\partial \bar{u}_j}{\partial x_j} = 0, \tag{3}$$

$$\frac{\partial \bar{u}_i}{\partial t} + \frac{\partial \bar{F}_{ij}}{\partial x_j} = \bar{S}_i, \tag{4}$$

$$\frac{\partial \bar{\rho}_*}{\partial t} + \frac{\partial \bar{R}_j}{\partial x_j} = 0, \tag{5}$$

where

$$\bar{F}_{ij} = \bar{u}_i \bar{u}_j + \bar{p}\delta_{ij} - \nu \frac{\partial \bar{u}_i}{\partial x_j} + \tau_{ij}, \tag{6}$$

$$\bar{S}_i = -(\bar{\rho}_* - \rho_b) g \frac{\partial x_3}{\partial x_i} + 2\Omega \left(\bar{u}_2 \frac{\partial x_1}{\partial x_i} - \bar{u}_1 \frac{\partial x_2}{\partial x_i} \right), \tag{7}$$

$$\bar{R}_j = \bar{u}_j \bar{\rho}_* - \kappa \frac{\partial \bar{\rho}_*}{\partial x_j} + \chi_j. \tag{8}$$

An overbar denotes that the corresponding quantity is grid filtered. In the above equations, $x_i (i = 1, 2, 3)$ denote the Cartesian coordinates in which x_1 and x_2 are the horizontal coordinates and x_3 is the vertical coordinate, t is time, $\bar{u}_i (i = 1, 2, 3)$

represent velocity components, $\bar{\rho}_*$ is the relative density deviation from a reference state, ρ_b denotes the relative background density, $\bar{p}$ is the reduced dynamic pressure, δ_{ij} is the Kronecker delta, ν is the kinematic viscosity, g denotes the gravitational acceleration, Ω is the angular velocity of the system, and κ denotes the thermal or molecular diffusivity.

The quantities τ_{ij} and χ_j in (6) and (8) are defined as

$$\tau_{ij} = \overline{u_i u_j} - \bar{u}_i \bar{u}_j, \tag{9}$$

$$\chi_j = \overline{u_j \rho_*} - \bar{u}_j \bar{\rho}_*, \tag{10}$$

and represent, respectively, the subgrid-scale stress and the subgrid-scale scalar flux. These two subgrid-scale quantities are modelled using the grid-filtered quantities with the dynamic subgrid-scale eddy viscosity model (Germano *et al.* 1991; Zang, Street & Koseff 1993*a*). In an eddy viscosity model, the subgrid-scale stress is modelled by an eddy viscosity which has a model coefficient (Smagorinsky 1963). Instead of having a prescribed model coefficient, the dynamic subgrid-scale eddy viscosity model is able to calculate the model coefficient using the resolved variables by filtering the governing equation at two different spatial scales. As a result, effects such as rotation, stratification and geometry on the unresolved subgrid-scale motion may be represented dynamically. In the present implementation, a local averaging together with a cutoff are used to stabilize the calculation. The readers are referred to Zang (1993) and Zang, Street & Koseff (1993*a*, *b*) for details of the derivation of the governing equations and the subgrid-scale models.

The governing equations are transformed into a non-orthogonal curvilinear coordinate system and discretized using a finite-volume approach in the computational domain. The non-staggered fractional-step method of Zang, Street & Koseff (1994) is employed to advance the equations in time. The present non-staggered method allows us to store only one set of metric quantities per control volume and as a result significantly reduces the memory requirement of the code. The pressure Poisson equation which is solved using an efficient multigrid method is formulated in the same manner as on a staggered grid so that the mass conservation can be satisfied to machine accuracy. The overall accuracy of the numerical method is second order in both space and time.

3. Problem definition

A schematic of the flow domain, the boundary conditions, and an illustration of the upwelled density interface and surface front are shown in figure 2. The geometries used in the present simulations are similar to those of NM87 except that, instead of a cylinder, a section of an annulus is employed, an approximation which will be justified in § 5. In some cases, a flat bottom instead of a sloping bottom is used. In total, six cases are considered in the present work. A summary of the geometric parameters and the grid resolution is given in table 1. In naming the cases, 'FB' and 'SB' represent, respectively, a flat bottom and a sloping bottom; axisymmetric cases are denoted by '2D', and three-dimensional cases are denoted by '3D'. In all cases, the outer radius R_0 is 0.45 m, and the inner radius R_1 is $0.1R_0$, which gives a horizontal length scale of the annulus $L_R = R_0 - R_1 = 0.405$ m. The span of the section of the annulus is defined by its included angle θ_0. The quantities H and h represent, respectively, the maximum and minimum depths of the section of the annulus (see figure 2). The grid points shown in table 1 are interior points. Two fictitious points outside the physical domain are added in each dimension in the calculations to facilitate implementing boundary

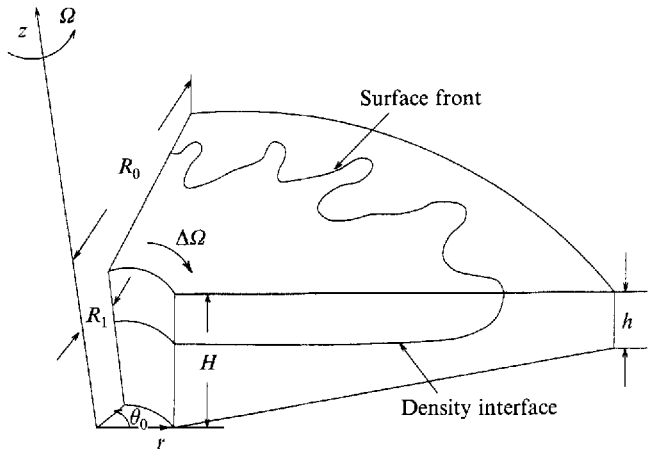

FIGURE 2. Schematic of the flow domain and the density interface.

Case	θ_0 (rad)	H (m)	h (m)	Grid resolution ($N_r \times N_\theta \times N_z$)	$\frac{\Delta r_{min}}{\overline{L_R}}$	$\frac{\Delta z_{min}}{\overline{H}}$	Time step Δt (s)
FB2D1	N/A	0.2	0.2	$128 \times 1 \times 96$	2×10^{-3}	1.5×10^{-3}	5×10^{-2}
FB2D2	N/A	0.2	0.2	$128 \times 1 \times 96$	1×10^{-3}	5×10^{-4}	5×10^{-2}
FB3D	$2\pi/3$	0.2	0.2	$64 \times 48 \times 64$	4×10^{-3}	4×10^{-3}	2.5×10^{-2}
SB3D1	$\pi/2$	0.15	0.033	$64 \times 64 \times 64$	4×10^{-3}	4×10^{-3}	2×10^{-2}
SB3D2	$\pi/2$	0.15	0.033	$64 \times 64 \times 64$	3×10^{-3}	3×10^{-3}	2×10^{-2}
SB3D3	$\pi/2$	0.15	0.033	$80 \times 80 \times 80$	2×10^{-3}	2×10^{-3}	1.5×10^{-2}

TABLE 1. The geometry and grid resolution for the simulation of upwelling flows in a section of an annulus with a sloping or a flat bottom.

conditions. The grid is non-uniform in the radial and vertical directions but uniform in the azimuthal direction. Grid points are clustered in the vicinity of solid walls. Geometric stretching is employed in the directions where grid distribution is non-uniform.

The governing equations are solved in the reference frame rotating with the container. The initial condition is that of a 'two-layer' stratified fluid with fresh water on top of salty water in solid-body rotation with the container. The initial density field, which approximates a two-layer stratified fluid, is taken to be horizontally uniform. Because we have invoked the Boussinesq approximation, the centrifugal force in the two layers is the same at the same radial locations. As a result, the density interface is flat under the static condition in the rotating reference frame. The vertical density profile is approximated by a hyperbolic tangent function. Since there was no information available on the thickness of the interface in the experiments, it was chosen to be as small as possible and yet large enough to be resolved by the computational grid. The number of grid points within the interface typically ranges from five to ten.

At time $t = 0$, upwelling flow is generated by relative rotation of the top lid, which simulates a wind stress. A no-slip condition for the velocity is applied to the top, bottom, inner, and outer walls. A no-flux condition is used for the density at the solid walls. At the two azimuthal boundaries, periodic boundary conditions are applied.

The physical parameters of the present cases are summarized in table 2. The Rossby number ϵ is based on the maximum lid velocity U_p and the radial span of the annulus

Case	$\epsilon = U_p/fL_R$	$E = \nu/fH^2$	$F_1 = f^2\lambda_s^2/g'h_{10}$	$\mathscr{R}/L_R$	t_s (s)
FB2D1	0.08	1.5×10^{-5}	2.9	0.10	202.4
FB2D2	0.07	8.3×10^{-6}	39.7	0.06	124.9
FB3D	0.07	1.0×10^{-4}	39.7	0.06	39.5
SB3D1	0.07	1.9×10^{-4}	39.7	0.06	39.5
SB3D2	0.04	1.2×10^{-4}	162.2	0.03	45.2
SB3D3	0.04	1.2×10^{-4}	162.2	0.03	45.2

TABLE 2. The physical parameters of upwelling flows in a section of an annulus.

L_R. The quantity $f = 2\Omega$ is the Coriolis parameter. The value of ϵ, which measures the strength of advection relative to rotation, is less than 0.1 in all cases. The Ekman number E, which is based on the kinematic viscosity ν, the Coriolis parameter and the maximum depth of the container H, is of the order of 10^{-5} for the axisymmetric cases and of 10^{-4} for the 3D cases, respectively. The internal Froude number of the upper layer F_1, which measures the strength of rotation relative to stratification, is much larger than $O(1)$ in all cases except Case FB2D1. In the definition of F_1 in table 2, λ_s is the theoretical stationary width of the density front (to be defined in §5), $g' = g(\rho_2 - \rho_1)/\rho_1$ is the reduced gravity. The values of the Rossby radius of deformation for the two-layer system, $\mathscr{R}$, are much smaller than L_R, which means that the effect of the inner wall of the annulus on the rotation-dominated flow structures near the outer wall is small. The spin-up time scale is defined by Linden & van Heijst (1984) as $t_s = (h_{10}/\Delta\Omega)((\Omega + \Delta\Omega)/\nu)^{1/2}$. The fluid is salt stratified with a Prandtl number of 723.

In the two axisymmetric cases, all the physical parameters of Cases FB2D1 and FB2D2 match, respectively, those of Cases (*e*) and (*b*) of Narimousa, Maxworthy & Spedding (1991). In the 3D cases, except for fluid viscosity, Cases FB3D and SB3D1 have the same physical parameters as Case (*b*) of Narimousa *et al.*, while Cases SB3D2 and SB3D3 match their Case (*a*). The fluid viscosity in the 3D cases is 12.5 times larger than that in the experiments, a necessary approximation which will be justified in §4. The parameters of Cases SB3D2 and SB3D3 are identical except a finer $80 \times 80 \times 80$ grid is used for SB3D3 in order to examine the effect of grid resolution.

NM87 defined a parameter $\theta^* = g'h_{10}/u_* f\lambda_s$, where u_* is the disk friction velocity. By using θ^*, which combines the effects of stratification, rotation, and surface stress, Narimousa & Maxworthy successfully correlated their data which span a wide range of parameters. However, through u_*, θ^* is a function of the fluid viscosity. Since the viscosity used in the present 3D computations is larger than that in their experiments, and scaling relations based on θ^* may not be independent of viscosity, it is difficult to compare the present data with the measured data based on θ^*. In fact, the present results do not seem to agree with the experimental data when they are scaled with θ^*. Therefore, quantitative comparisons with the experiments will be based on inviscid parameters which are given in §5.

The primary length scale in the vertical direction of NM87 is the thickness of the Ekman layer. We denote the thickness of a laminar Ekman layer as δ_E^l and the thickness of a turbulent Ekman layer as δ_E^t. The scaling relations for δ_E^l (Greenspan 1968) and δ_E^t (Caldwell, Van Atta & Helland 1972) are

$$\delta_E^l \sim (\nu/f)^{1/2}, \tag{11}$$

$$\delta_E^t \sim u_*/f, \tag{12}$$

where $f = 2\Omega$ is the Coriolis parameter and Ω is the angular velocity of the system rotation. The quantity u_* which is called the disk friction velocity is defined as

$$u_* = (\tau_w/\rho)^{1/2}, \tag{13}$$

where τ_w is the shear stress at the disk.

Although the Ekman layer may become turbulent at small Ekman numbers, it is laminar during the initial spin-up process. In the present upwelling flows, the top Ekman layer is laminar until baroclinic instability occurs near the surface, at which time the Ekman layer breaks down. As a result, we take the laminar Ekman layer thickness as the vertical length scale. In the present analysis, the laminar Ekman thickness is also used to determine the cross-shore length scale near the radial boundary.

Since the instability of the surface density front is of interest, the length scale of the frontal waves determines the spatial resolution in the circumferential direction. From past experimental data, the size of the saturated frontal waves or eddies scales with the geometric mean of the Rossby deformation radii of the two layers as

$$L_w/2\pi\hat{R} = C_L, \tag{14}$$

where the value of C_L is close to 1.1 (Griffiths & Linden 1982; Chia, Griffiths & Linden 1982; Phillips 1954; Killworth, Paldor & Stern 1984; NM87).

The time scale of the upwelling flow, which is the time period between the start of the 'wind' and the time when the upwelled surface front reaches the stationary state was estimated by NM87 as

$$t_s = 3.1\left(\frac{\lambda_s g' h_0}{u_*^3 f}\right)^{1/2}, \tag{15}$$

where $g' = g(\rho_2 - \rho_1)/\rho_1$ is the reduced gravity, and h_0 is the initial depth of the upper layer.

Based on the above length and time scales, spatial and temporal resolutions may be determined and the feasibility of an LES may be assessed. In the following, a brief discussion is given on the feasibility of the simulation and the necessary approximations. A detailed analysis can be found in Zang (1993).

We pick one particular experiment, Case (*a*) of Narimousa *et al.* (1991) which we refer to as Case SCALE, to perform our scaling analysis. If a geometrically stretched grid is employed in both the radial and the vertical directions with five grid points within the top and bottom Ekman layer and the sidewall boundary layer, and a uniform grid is used in the circumferential direction with six grid points within one frontal wave, the grid will contain about 3.1 million grid points based on the length scales in (11) and (14). In the present upwelling flow simulations, we need to store about 60 variables per grid point (Zang *et al.* 1994; Zang 1993). The computer memory requirement amounts to about 190 million words. Comparing with the 64 million word central memory of the Cray YMP on which the upwelling runs were executed, we observe that the storage of the above grid in the main memory is not possible.

The number of time steps required to reach the stationary state is approximately 40000 based on the time scale in (15). The estimated CPU time per grid point per time step using one processor of a Cray Y-MP is about 45 μs for the present run (Zang *et al.* 1994; Zang 1993). Putting these numbers together we obtain the required total CPU time for one run to be about 1900 hours which is too expensive.

As stated in §3, two approximations were made in order to yield a feasible problem for numerical simulation. One is to increase the fluid viscosity, i.e. increase the Ekman number or reduce the Reynolds number. In the present simulation, we employ a fluid viscosity that is 12.5 times larger than that of water, i.e. $\nu = 1.25 \times 10^{-5}$ m^2 s^{-1}. If the fluid viscosity is too large, the flow becomes completely laminar and the frontal waves are dissipated. The other approximation is to simulate upwelling in a section of an annulus instead of a cylinder to reduce the azimuthal extent of the domain. Since the phenomena of interest such as upwelling and frontal stability are located near the outer boundary and are far away from the centre of the cylinder, the addition of a small inner wall in the annulus does not have a significant effect. This is confirmed by the results in §5.

After the above two approximations, a grid of 66 points in each direction is sufficient and the estimated computer memory is 17 million words and the total CPU time on one processor of the Cray Y-MP is about 15 hours. While it is still very expensive, the present simulation only requires less than 1% of the CPU time that would be consumed by a simulation of the actual NM87 experiment. As is shown in the following section, the present simulations have reproduced most of the interesting features observed in NM87.

5. Simulation results

5.1. *Qualitative description*

A qualitative picture of the evolution and structure of the upwelling flow is described for Case SB3D2. The situation in other cases is similar. A large amount of information is extracted by examining the flow field through the use of computer animation. In the following, terminology from physical oceanography is occasionally used for convenience. The direction toward the axis of the annulus is called the 'seaward' direction, while that toward the outer wall is called the 'shoreward' direction. 'Longshore' refers to the azimuthal direction, and 'cross-shore' represents the radial direction. A radial–vertical plane is called a 'cross-shore' plane, while an azimuthal–vertical plane is called a 'longshore' plane. A cyclone (anticyclone) is a flow structure whose relative vorticity has the same (opposite) sign as the Earth or the system rotation.

As the lid rotates clockwise relative to the anticlockwise system rotation ($\Delta\Omega < 0$), fluid near the top which moves with the lid is driven radially inward by the Coriolis force and forms the top Ekman layer, which is established within one rotation period. Constrained by mass conservation, fluid returns to the outer wall below the Ekman layer, which occurs at first in the interior of the flow. This forms a secondary cross-shore circulation in the radial–vertical plane. Initially, this circulation consists of one cell which rotates counter-clockwisely when viewed in the positive azimuthal direction. Because there is no azimuthal pressure gradient, as the flow adjusts to the geostrophic balance, radial transport in the interior weakens. At the same time, the bottom Ekman layer and the sidewall boundary layers develop and establish a cross-shore secondary circulation. These adjustments occur in a time scale of 5 to 10 rotation periods.

The upward vertical transport near the outer wall lifts up the density interface there. The peak of the interface corresponds to the location where the vertical velocity is

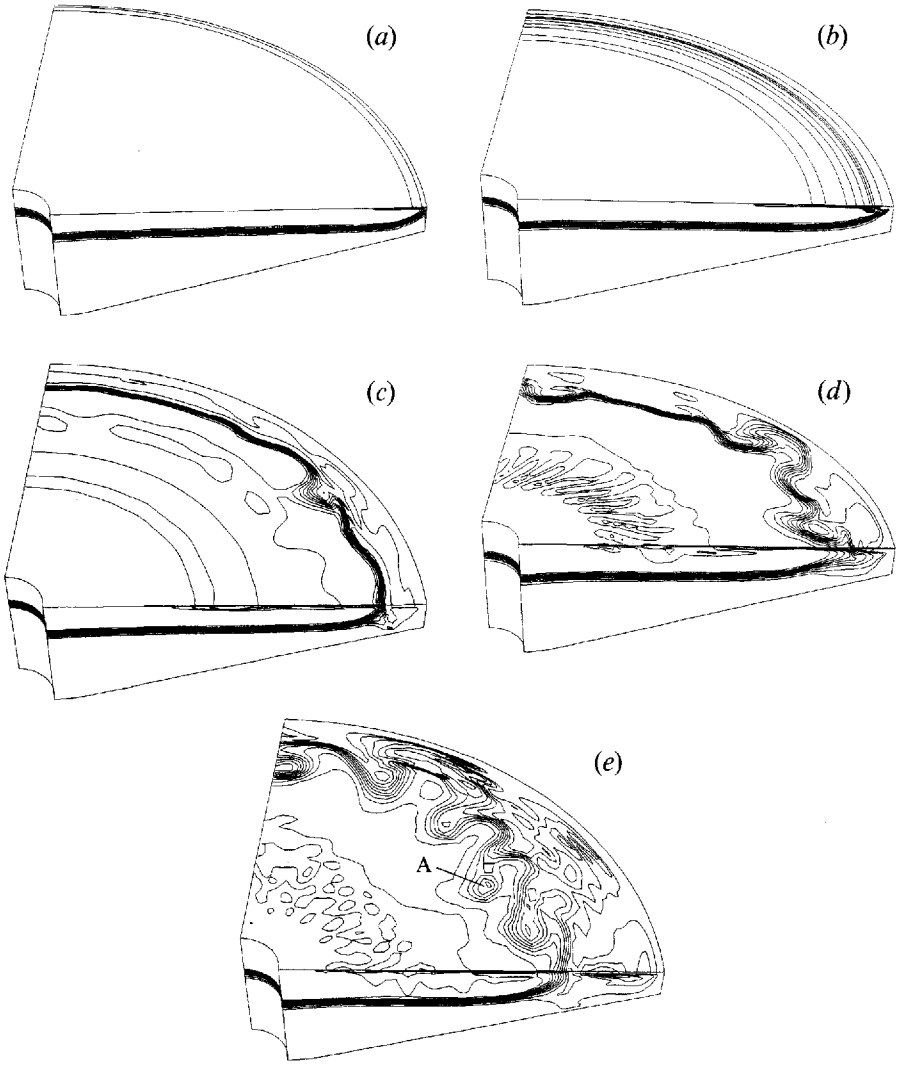

FIGURE 3. Density field ρ/ρ_2: (*a*) $t/t_s = 0.25$, the main body of the interface has yet to touch the top surface; (*b*) $t/t_s = 0.5$, axisymmetric front; (*c*) $t/t_s = 0.9$, small-amplitude waves appear at the front; (*d*) $t/t_s = 1.5$, frontal waves grow to large amplitude; (*e*) $t/t_s = 2.0$, frontal waves saturate and eddies break away from the front (point 'A'). (Case SB3D2.)

maximum in the sidewall boundary layer. When this peak reaches the top Ekman layer, it is carried radially inward by the Ekman transport. Figure 3(*a*) shows the density field when the non-dimensional time t/t_s is at 0.25. We can see that a thin layer of interface fluid which is slightly heavier than the upper-layer fluid (which one might call the 'top inversion layer') develops near the top, before the main body of the interface touches the surface.

If the relative rotation of the top lid is strong enough, the body of the interface will intersect the surface and form an axisymmetric surface front (referred to as the 'primary front'). At $t/t_s = 0.5$ (figure 3*b*), the main body of the interface has just reached the top surface. The 'nose' of the top inversion layer has moved further offshore. At the immediate sea side of the interface, there is a 'blob' of interface fluid which is dropping down as it is shown in the radial–vertical cross plane. Actually the 'blob' is an axisymmetric column of sinking fluid due to the unstable stratification (see

§5.3 and figure 5 for more discussion). The axisymmetric primary front of this moment is still in its forming stage which is relatively wide.

At $t/t_s = 0.9$ (figure 3*c*), small-amplitude azimuthal waves have appeared at the primary front while the front is almost axisymmetric. Seaward of the primary front, there is another axisymmetric but weaker front (the 'secondary front') which forms the nose of the top inversion layer. The top inversion layer moves farther offshore than the primary front and becomes thicker in the process owing to diffusion. On the shoreside of the primary front, there is an intensive mixing zone below the top Ekman layer, which one might call the 'trailing mixing zone'. This zone is created by the circulation between the outer wall and the front. As the lower-layer fluid is lifted up in the boundary layer on the outer wall, it is transported radially inward in the top Ekman layer. When reaching the density front, the lower-layer fluid begins to sink back down because of unstable stratification. This sinking motion drags a portion of the interface fluid with it and creates intensive mixing. At this time, the cross-shore circulation consists of two main cells separated by the density interface. The two cells rotate counterclockwisely when viewed in the direction opposite to the lid velocity (the 'poleward direction'). The two-cell structure and the 'sinking' behaviour of the upwelled fluid near the front are consistent with the observations of Mooers *et al.* (1976).

As the front migrates offshore, it becomes unstable to small perturbations and azimuthal frontal waves appear and grow (cf. the observations of Petrie *et al.* 1987 with respect to the baroclinic waves in the western-boundary upwelling off Nova Scotia). As shown in figure 3(*d*), which is at $t/t_s = 1.3$, the initially axisymmetric front has evolved into an irregular pattern with large-scale frontal waves and eddies. The surface front is much wider at the location of the frontal eddies owing to the strong eddy transport and mixing. The top inversion layer becomes unstable and begins to sink to the lower layer. The previously axisymmetric secondary front splits into azimuthal bands which emanate from the secondary front. A total of eight bands is observed which gives a circumferential wavenumber of 32.

The frontal waves grow to large amplitude and eventually become saturated. The structure of the saturated waves which is shown in figure 3(*e*) at $t/t_s = 2.0$ consists of cyclone/anticyclone pairs which form jet-like structures at their boundaries. At the crest of the second wave (point A in figure 3*e*), we see that a cyclonic vortex is breaking off from the main front and becoming a 'pinched-off' cyclone. The structures of cyclone/anticyclone pairs, jets and pinched-off cyclones were also observed in the flow visualization in NM87.

The thickness of the front is larger owing to mixing on both sides. In the cross-shore plane, the trailing mixing zone extends from the shoreside of the front all the way to the outer wall boundary layer. Because of the propagation of azimuthal waves, the cross-shore flow structure becomes very unsteady (compare figures 3*d* and 3*e*). The cross-shore transport in a vertical cross-section changes rapidly as azimuthal waves pass through. At this time, the azimuthal bands at the unstable top inversion layer have broken into isolated patches of interface fluid which eventually descend back down to the lower layer. The structure of instabilities of the primary and the secondary fronts will be discussed in more detail in §5.3.

5.2. *Quantitative comparisons with past results*

5.2.1. *Front-surfacing time* t_f

When the surface stress is strong enough, the density interface intersects the top lid and forms a surface front. The time scale for the front to appear at the top surface is

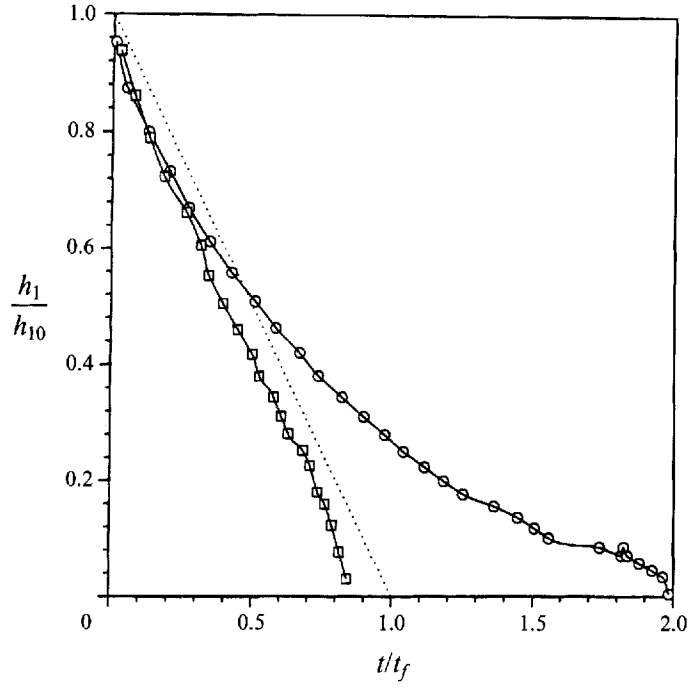

FIGURE 4. Time history of the height of the interface. Symbols are: —○—, Case FB2D1; —□—, Case FB2D2; straight line connects (0, 1) and (1, 0), plotted for reference.

Case	Yoshida (1955) t_f/t_s	Present t_f/t_s	Present u_* (cm s^{-1})
FB2D1	0.29	0.58	0.60
FB2D2	0.31	0.26	0.64
FB3D	0.30	0.29	1.0
SB3D1	0.37	0.43	1.0
SB3D2	0.27	0.33	1.1
SB3D3	0.27	0.26	1.1

TABLE 3. The surfacing time of the front t_f/t_s and the computed disk friction velocity u_*. Refer to tables 1 and 2 for details of the runs.

denoted by t_f. The computed values of t_f/t_s are compared with Yoshida's (1955) analytical criterion (equation (1)) and the results are shown in table 3. Also shown in table 3 is the computed value of the disk friction velocity u_*.

Agreement between the computed and the analytically predicted front-surfacing time is reasonably good except for Case FB2D1. The fine-grid result of Case SB2D3 agrees better with Yoshida's prediction than Case SB2D2. In Case FB2D1 the Froude number F_1 is of order one while values of F_1 in the other cases are much larger (table 2). This indicates that, in Case FB2D1, the time scale of buoyancy is comparable to that of rotation. Therefore it is possible that the buoyancy effect may have become important in this case before the interface touches the top lid. Moreover, the nonlinear terms may also be of significance in this time scale. These may invalidate the balance assumed in Yoshida's model. To verify this, we plot the time history of the upper-layer depth at the outer wall in figure 4 for Cases FB2D1 and FB2D2. Based on Yoshida's theory, h_1/h_{10} should decrease linearly *vs.* time. In figure 4, the dotted straight line is

Case	λ_s/L_R Theory (equation (16))	λ_s/L_R Present	$\lambda_s/\mathscr{R}_s$ Present
FB2D1	0.17	0.14	1.5
FB2D2	0.37	0.34	7.0
FB3D	0.37	0.44	9.0
SB3D1	0.37	0.40	8.1

TABLE 4. The width of the stationary front.

plotted for reference. We see that while the curve of Case FB2D2 is almost straight, the curve of Case FB2D1 deviates from linear trend when t is larger than about $0.3t_f$. This deviation from a linear trend shows that (1) is valid at large Froude numbers but may not be valid when the Froude number is of order one.

5.2.2. *Stationary-front width* λ_s

As the front is driven by the Coriolis force and migrates offshore, its curvature increases. As a result, a pressure gradient begins to build up across the front. At some stage, this radial pressure gradient balances the Coriolis force and the front stops migrating and becomes stationary. The stationary-front width λ_s measured from the outer wall is compared with an analytical result which is based on the geostrophic balance between the Coriolis force and the cross-front pressure gradient. Derivations of the expression for λ_s for a cylinder may be found in Narimousa & Maxworthy (1985) and, in a somewhat different form, in Linden & van Heijst (1984). The formula for λ_s in an annulus is derived in the Appendix:

$$\lambda_s = R_0 - \left\{ R_1^2 + \left[\frac{4g' h_0 (R_0^2 - R_1^2)}{f \Delta \Omega} \right]^{1/2} \right\}^{1/2}. \tag{16}$$

Table 4 shows the values of λ_s/L_R and $\lambda_s/\mathscr{R}_s$, where $\mathscr{R}_s$ denotes the two-layer Rossby radius of deformation defined in (2) and computed at the stationary-front location. Results from Cases SB3D2 and SB3D3 are not available since these were not run long enough to reach a stationary state. In the 3D simulations, the λ_s value is the averaged width of the stationary front.

We see that the computed values of λ_s agree very well with the theoretical result based on geostrophic balance. This agreement is consistent with the experimental results of NM87.

Table 4 shows that the values of $\lambda_s/\mathscr{R}_s$ are generally larger than one. The present results as well as those from NM87 show that λ_s is larger at smaller $\mathscr{R}$, which indicates that the front width is not only a function of rotation and stratification, but is also strongly dependent on the magnitude of the surface stress.

5.2.3. *Wavelength of the saturated waves*

As the surface front migrates offshore, it is unstable to azimuthal perturbations. Waves develop at the front and grow to large amplitude. At some stage, the waves stop growing and become saturated. The stability of a density front has been investigated experimentally by Hide (1971), Hart (1980), Griffiths & Linden (1981, 1982), Linden & van Heijst (1984), Sanders (1973), Chia *et al.* (1982), and NM87, among others. Theoretical stability analyses have been carried out by Eddy (1949), Phillips (1954), Griffiths & Linden (1981), and Killworth *et al.* (1984). For fronts sufficiently far from

Case	Experiment (NM87)	Present
FB3D	N/A	1.19
SB3D1	1.22	1.04
SB3D2	0.98	1.00

TABLE 5. The dimensionless wavelength of the saturated waves.

Case	Theory (Phillips 1954)	Computation (Present)
FB3D	0.30	0.41
SB3D1	0.40	0.39
SB3D2	0.42	0.46
SB3D3	0.42	0.44

TABLE 6. The dimensionless wave speed u_w/U_θ, where U_θ is the local lid velocity.

a wall, it was found that the wavelength of the most unstable mode L_w scales linearly with the geometric mean of the deformation radii of the two layers, $\hat{R} = (\bar{R}_1 \bar{R}_2)^{1/2}$, where $\bar{R}_i = (g' h_i)^{1/2}/f (i = 1, 2)$.

Table 5 shows the dimensionless saturated wavelength $L_w/2\pi\hat{R}$ from the present computation and the experiment of NM87. The values of NM87 in table 5 were calculated from their published data. The data from Case SB3D3 are not available because it was not run long enough to reach the stage of saturated waves. Reasonable agreement has been achieved between the computation and the experiments. The discrepancies are within the experimental uncertainty in NM87 which is about 10 to 20%. The values of $L_w/2\pi\hat{R}$ are also consistent with previous findings. For example, the experiment of Griffiths & Linden (1982) gives $L_w/2\pi\hat{R} = 1.1 \pm 0.3$, Chia *et al.* (1982) gives 1.16 ± 0.27, Phillips' (1954) gives 1.08, and the model of Killworth *et al.* (1984) gives 1.15.

5.2.4. *Drift speed of the frontal waves*

The frontal waves drift in the direction of the applied stress. Phillips' (1954) model predicts that the wave speed of the baroclinic waves u_w is

$$u_w = [U_1(K^2 + 2F_2) + U_2(K^2 + 2F_1)]/2(K^2 + F_1 + F_2), \tag{17}$$

where U_1 and U_2 are the mean longshore velocity of the upper and lower layers, respectively, F_1 and F_2 are the layer Froude numbers defined as $F_i = f^2\lambda_s^2/g'\bar{h}_i (i = 1, 2)$, $\bar{h}_i$ is the averaged layer depth, and $K = (k^2 + l_j^2)^{1/2}$ is the total wavenumber, where $l_j = (j + \frac{1}{2})\pi (j = 0, 1, 2, \ldots)$.

In table 6, the computed u_w/U_θ and the theoretical value from the above equation are shown, where U_θ is the disk velocity at the front. Phillips' model predicts that the most unstable mode has a cross-shore wavenumber $l_j = \pi/2$ $(j = 1)$. Thus, in calculating the value of K in (17), l_j is $\pi/2$, k is taken as the computed azimuthal wavenumber of the frontal waves, and U_1 and U_2 are the computed mean velocities of the upper and lower layers, respectively. We can see that good agreement is obtained between the computation and Phillips' prediction for the three cases with a sloping bottom. Notably, the value of u_w from the coarse-grid calculation Case SB3D2 is within 5% of that from Case SB3D3 under the same flow conditions but with a fine

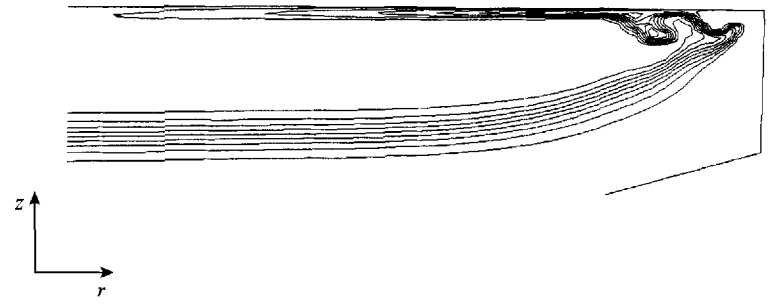

FIGURE 5. Blown-up view of the sinking of the interface fluid and the formation of the surface front.

grid. The computed wave speed for the flat-bottom case (FB3D) is larger than the inviscid theoretical prediction by 30%. The discrepancy may be due to the fact that Phillips' theory is quasi-geostrophic with no front while the present calculation simulates frontal dynamics with a large viscosity.

Compared to the measurements of NM87 which give

$$u_w = 0.5U_1 = 0.37U_\theta, \tag{18}$$

the present computation gives a larger u_w. The value of U_1/U_θ is 0.74 in NM87, while in the computations, it ranges from 0.42 to 0.46, which means that the wave speed is almost equal to the mean speed of the upper layer. Notice that from (17), if $F_1 \approx F_2$, then $u_w \approx (U_1+U_2)/2$. Therefore, (18) indicates that $U_2 \ll U_1$ in the experiments of NM87. In the present cases, however, U_2/U_1 is only slightly smaller than unity (see figure 7 in the next subsection), which results in $u_w \approx U_1$. We conjecture that because the interface was thinner and the viscosity smaller in the experiments, a larger shear between the two layers was supported, which resulted in a smaller U_2 in NM87.

5.3. *Structure of the upwelling and frontal waves*

Having compared the simulation to past experimental and theoretical results and validated our simulation, we may study the structure of the upwelling flow and the frontal instabilities in more detail. Examination of the detailed three-dimensional flow and density fields from the numerical simulations allows us to show explicitly the evolution of the upwelling and the three-dimensional structure of the frontal vortices which previously could only be inferred from field observations and laboratory experiments. We will focus primarily on the discussion of Case SB3D2 since it possesses the most prominent features of the frontal waves. Good agreement between results from Case SB3D2 and Case SB3D3 where a finer grid was used verified that the grid resolution in Case SB3D2 was sufficient to resolve the flow structures of interest. Unless otherwise noted, the following description is about Case SB3D2.

5.3.1. *Cross-shore structure*

As the interface is lifted up near the outer wall by the upwelling, its peak, which corresponds to the location of the maximum vertical velocity in the sidewall boundary layer, first reaches the top surface and enters the top Ekman layer. The interface fluid in the peak is transported seaward by the Ekman flux. As it crosses the interface and enters into the upper layer, this column of interface fluid experiences unstable stratification and begins to sink down (figure 5). The dropping fluid connects with the main interface as they meet. A circulation is thus formed in which the lower-layer fluid

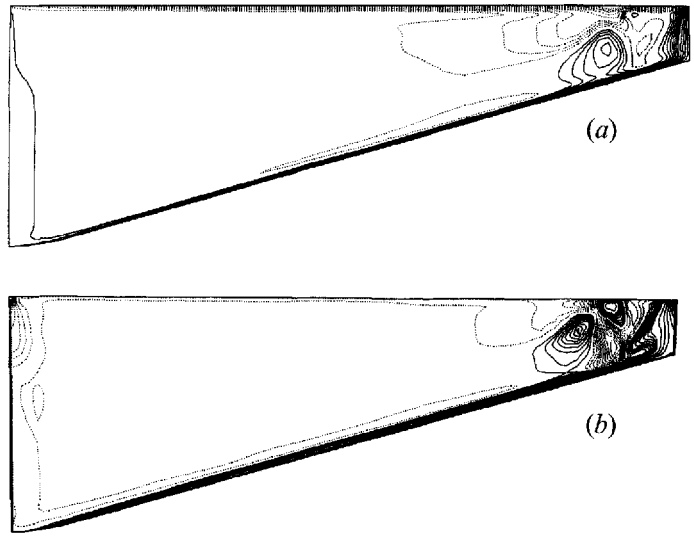

FIGURE 6. Contours in a cross-shore plane at $t/t_s = 0.9$. Dotted lines are negative contours. (*a*) Azimuthal velocity $(u_\theta - u_f)/U_p$, where u_f is the azimuthal speed of the front. Contours from -0.1 to 0.4. (*b*) Azimuthal vorticity $\omega_\theta/(U_p/R_0)$. Contours from -30.0 to 90.0. (Case SB3D2.)

is lifted up in sidewall boundary layer, carried seaward by the Ekman transport, and dropped down as it is crossing the interface. The surface front is therefore located where the lifted lower-layer fluid drops. This circulation at the shoreside of the front creates what we call the 'trailing mixing zone'.

After the interface touches the top lid, the cross-shore circulation is split into two main cells, with one in each layer. These two cells rotate counter-clockwise when viewed from downstream and are separated by the density interface. Figure 6(*a*) shows the azimuthal velocity field in a cross-shore plane at $t/t_s = 0.9$; the velocity of the front movement has been subtracted out. Solid lines represent positive contours values and dotted lines represent negative values. Relative to the front, the upper layer moves downstream while the lower layer goes upstream. Relative to the container, all the fluid moves in the direction of the wind stress and no reverse underflow is observed. Figure 6(*b*) shows the azimuthal vorticity in the same plane. At this time, most of the cross-shore motion occurs in the shore side of the front in the trailing mixing zone. These results are consistent with the observations of Mooers *et al.* (1976).

Figure 7 shows the profiles of the azimuthal velocity u_θ, radial velocity u_r, and density ρ along two vertical lines on the seaward side of the front. The first line (*a*) is very close to the front where the interface is curved up, while the second line (*b*) is seaward of the first line where the interface is essentially flat. We see that in (*a*), because of the horizontal density gradient, there is a shear in the azimuthal velocity across the interface. Shear also exists in the radial velocity profile across the interface, although it is very weak. On the other hand, in (*b*), where there is no horizontal density gradient, the velocity profiles are uniform. This is consistent with the thermal wind relation. The density profile shows a top inversion layer and a fairly sharp interface. The longshore velocity is in the direction of the applied stress. The radial velocity is very weak except in the top and bottom boundary layers. Examination of the top and bottom boundary layers shows that the Ekman layers are essentially laminar.

Figure 8(*a*) shows the velocity vector field in a vertical cross-section at $t/t_s = 1.3$, at which time frontal waves have already developed and the top inversion layer has begun to drop. The drop of the top inversion layer induces several azimuthal vortices.

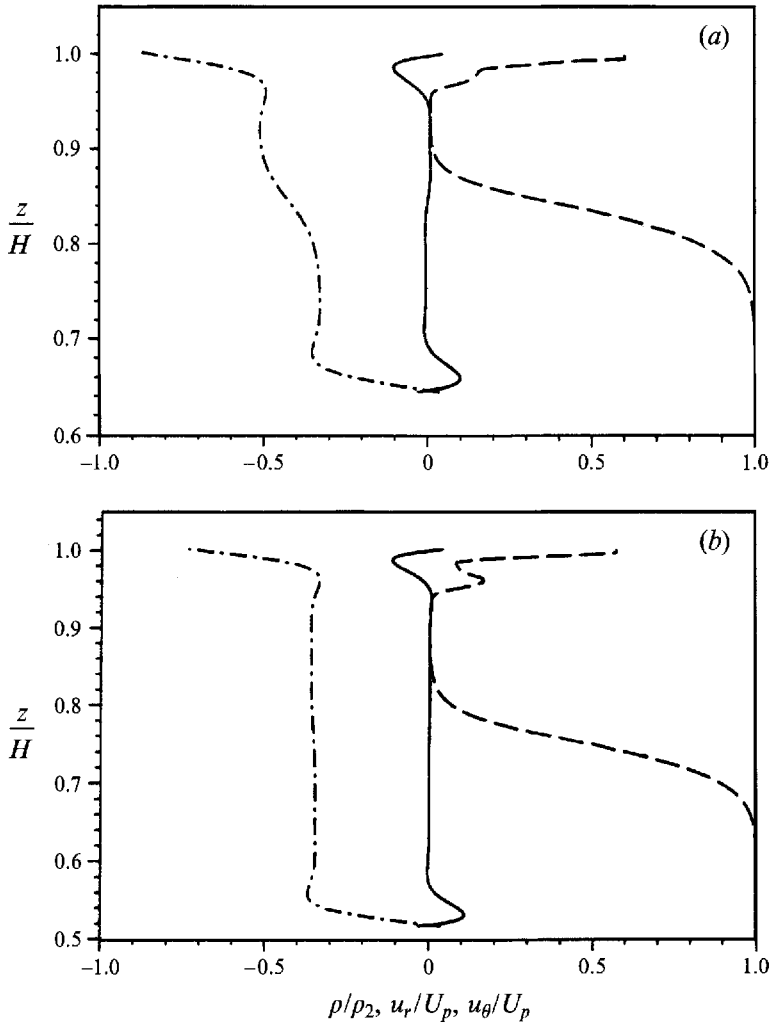

FIGURE 7. Profiles along vertical lines seaward of the front, $\theta/\theta_0 = 0$, and $t/t_s = 0.9$. Lines are: ——, u_r/U_p; — · —, u_θ/U_p; – – –, ρ/ρ_2, where U_p is the maximum speed of the lid. (*a*) $r/R_0 = 0.87$, (*b*) $r/R_0 = 0.75$. (Case SB3D2.)

Shoreside of the front, heavy fluid downwells from the top Ekman layer and creates an intensive mixing zone. We see that as frontal waves propagate through, the on- and offshore transport is no longer confined in the top and bottom boundary layers. Large radial velocity also occurs in the bulk region. In this cross-section, the upper-layer fluid below the top Ekman layer moves shoreward while the lower-layer fluid moves seaward. Figure 8(*b*) shows the velocity vector field in the same vertical cross-section at $t/t_s = 2.0$. We see that the cross-shore transport at this time is completely different from the previous picture. On the sea side of the front, seaward-moving upper-layer fluid is compensated by the shoreward-moving lower fluid. However, on the shore side of the front, the whole bulk fluid moves shoreward. This result shows that as pairs of cyclonic and anticyclonic frontal waves pass through, the cross-shore transport in a vertical plane is very unsteady and changes dramatically.

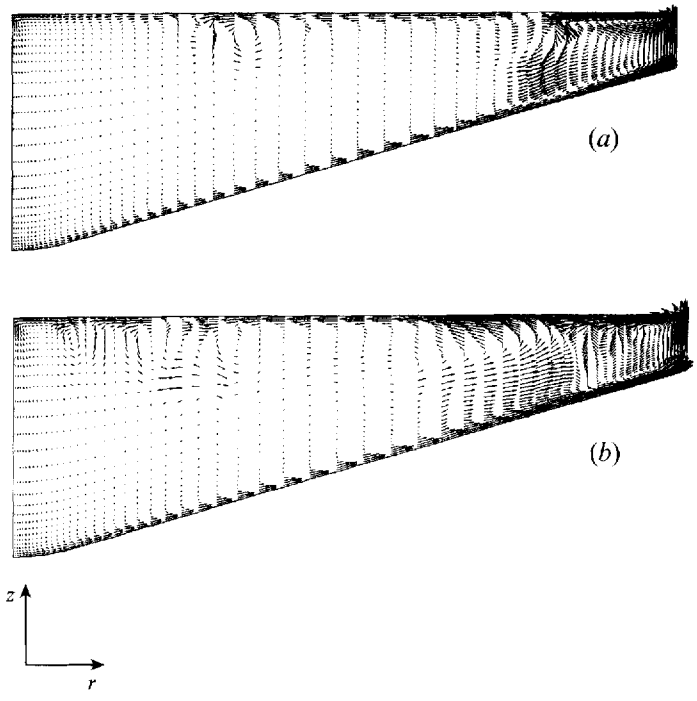

FIGURE 8. The velocity field in a cross-shore plane: (*a*) $t/t_s = 1.3$; (*b*) $t/t_s = 2.0$. (Case SB3D2.)

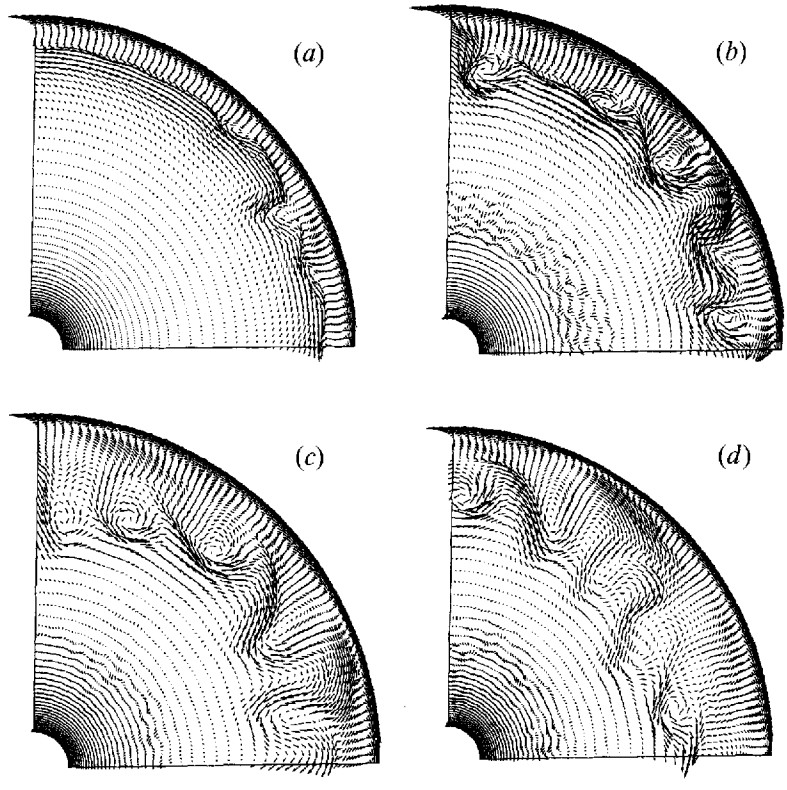

FIGURE 9. Velocity vector field in a horizontal plane just below the top Ekman layer, at $z/H = 0.95$. The reference frame is travelling with the frontal waves. (*a*) $t/t_s = 1.0$; (*b*) $t/t_s = 1.3$; (*c*) $t/t_s = 1.8$; (*d*) $t/t_s = 2.0$. (Case SB3D2.)

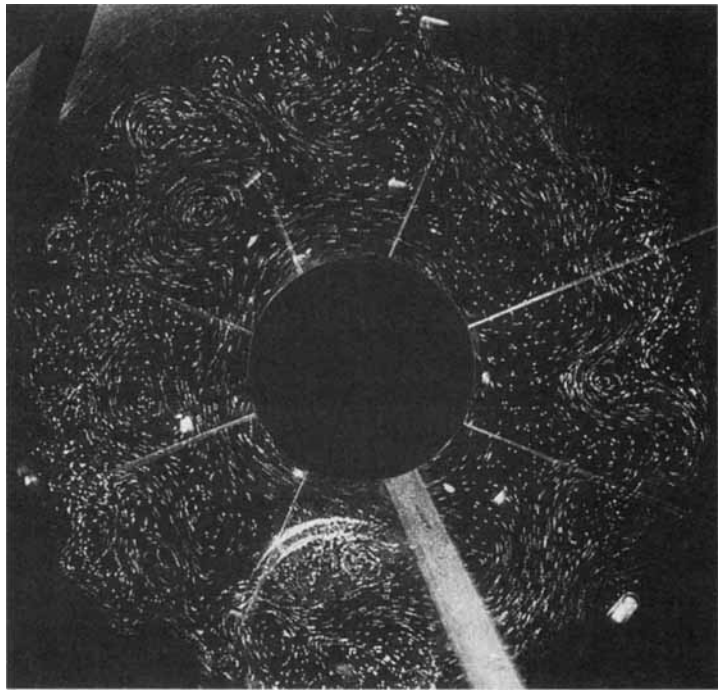

FIGURE 10. Frontal eddies in a laboratory experiment (Case *a* of Narimousa *et al.* 1991).

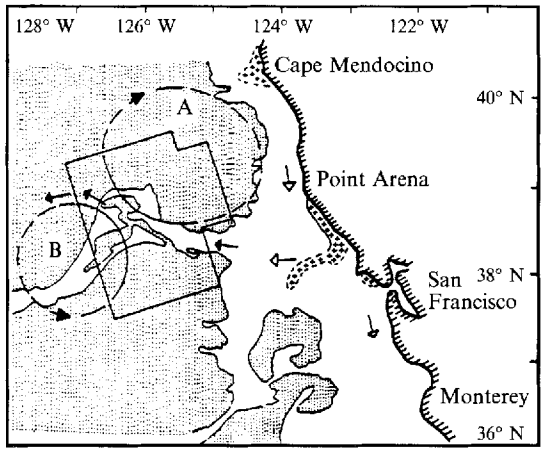

FIGURE 11. Eddies and jet-like structure at the coastal upwelling front (Mooers & Robinson 1984).

5.3.2. *Horizontal structure*

We now examine the flow structures in the horizontal plane. Figure 9(*a–d*) shows the evolution of the velocity field from $t/t_s = 1.0$ to 2.0 in the plane $z/H = 0.95$. The velocities are plotted in the reference frame travelling with the frontal waves in order to reveal their structures. We see that the waves first appear only at the front location (figure 9*a*) but extend to the container wall as they grow to large amplitude. After $t/t_s = 1.8$, the waves appear to be saturated. High-speed jets which transport heavy fluid offshore are formed at the upstream edge of the cyclonic regions. The structure closely resembles that observed through flow visualizations in NM87 (figure 10). It is

also similar to the structure observed by Mooers & Robinson (1984) in the California Current system (see figure 11).

Let the x-axis point toward the coast and the y-axis point along the coast against the wind direction. The vertical component of the relative vorticity ζ_r is defined as

$$\zeta_r = \frac{\partial v}{\partial x} - \frac{\partial u}{\partial y}.$$

Contours of ζ_r at $t/t_s = 2.0$ and $z/H = 0.95$ are plotted in figure 12(*a*), and the vertical velocity w in the same plane is shown in figure 12(*b*). The frontal waves appear in the form of cyclone/anticyclone pairs. In the following, we call a wave crest the farthest offshore location of a wave and a wave trough the nearest offshore location. We see that at the primary front, wave crests correspond to cyclonic regions while wave troughs correspond to anticyclonic regions. In addition, since the crests enclose lower-layer fluid, they also correspond to downwelling. In contrast to this, wave troughs correspond to regions where upper-layer fluid upwells on the seaward side of the front.

Figure 13(*a*) shows profiles of u_θ, $10w$, and ρ at $t/t_s = 0.9$ along a radial line below the top Ekman layer. Figure 13(*b*) is a similar plot at $t/t_s = 2.0$. Notice that the vertical velocity is increased by a factor of 10 for plotting purposes. We see that the magnitude of the longshore velocity u_θ has two maxima. One corresponds to the edge of the sidewall boundary layer, and the other, which is the true maximum, always occurs at the location of the surface front. Fluid rises in the outer-wall boundary layer and descends in the inner-wall boundary layer. There is strong downwelling on the shoreward side of the front and upwelling on the seaward side. The fluctuations which appear close to the inner wall at $t/t_s = 2.0$ correspond to the instability of the secondary front and the drop of the top inversion layer. We see that there is an anti-correlation between the density and the vertical velocity which signals the dropping of the heavy fluid and rising of the light fluid.

The structure of the longshore (azimuthal) velocity is of special interest. It has been observed by many researchers that the longshore velocity in the upper layer has a coastal jet structure. O'Brien & Hurlburt (1972) provided an explanation of the existence of the jet based on the conservation of potential vorticity. Consider a two-layer fluid system and assume that the coast is a straight line. Neglecting the longshore gradient of the cross-shore velocity, we can write the potential vorticity equations for the two layers as

$$\frac{\mathrm{d}}{\mathrm{d}t}\left(\frac{\partial v_1/\partial x + f}{h_1}\right) = 0, \tag{19}$$

$$\frac{\mathrm{d}}{\mathrm{d}t}\left(\frac{\partial v_2/\partial x + f}{h_2}\right) = 0. \tag{20}$$

The above equations can be integrated in time. Assuming that the fluid is at rest initially, we have

$$\frac{\partial v_1}{\partial x} - f\left(\frac{h_1 - h_{10}}{h_{10}}\right) = 0, \tag{21}$$

$$\frac{\partial v_2}{\partial x} - f\left(\frac{h_2 - h_{20}}{h_{20}}\right) = 0. \tag{22}$$

When upwelling occurs, $h_1 < h_{10}$ and $h_2 > h_{20}$. Thus, in the geostrophic region, $\partial v_1/\partial x < 0$ and $\partial v_2/\partial x > 0$. However, $v_1 = 0$ at the coast and since $v_1 < 0$ in the upwelling region, $\partial v_1/\partial x > 0$ in the coastal boundary layer. Therefore, v_1 must have a

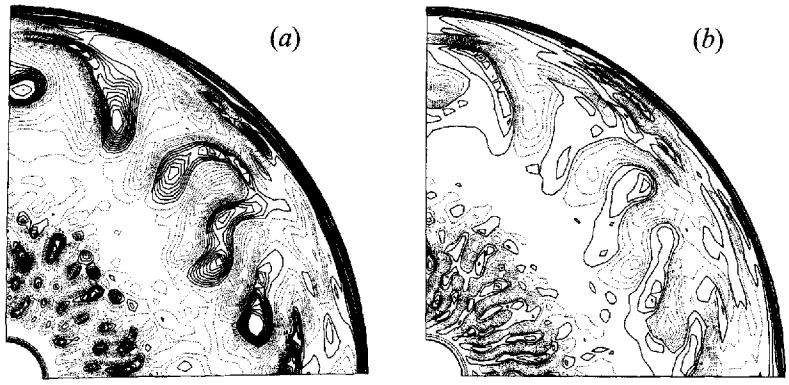

FIGURE 12. Contours in a horizontal plane just below the top Ekman layer, at $z/H = 0.95$ and $t/t_s = 2.0$. Solid lines represent positive values, and dotted lines represent negative values. (*a*) Vertical relative vorticity $\zeta_r/(U_p/R_0)$. Contour values are from -7.5 to 39. (*b*) Vertical velocity w/U_p. Contour range from -0.06 to 0.08. (Case SB3D2.)

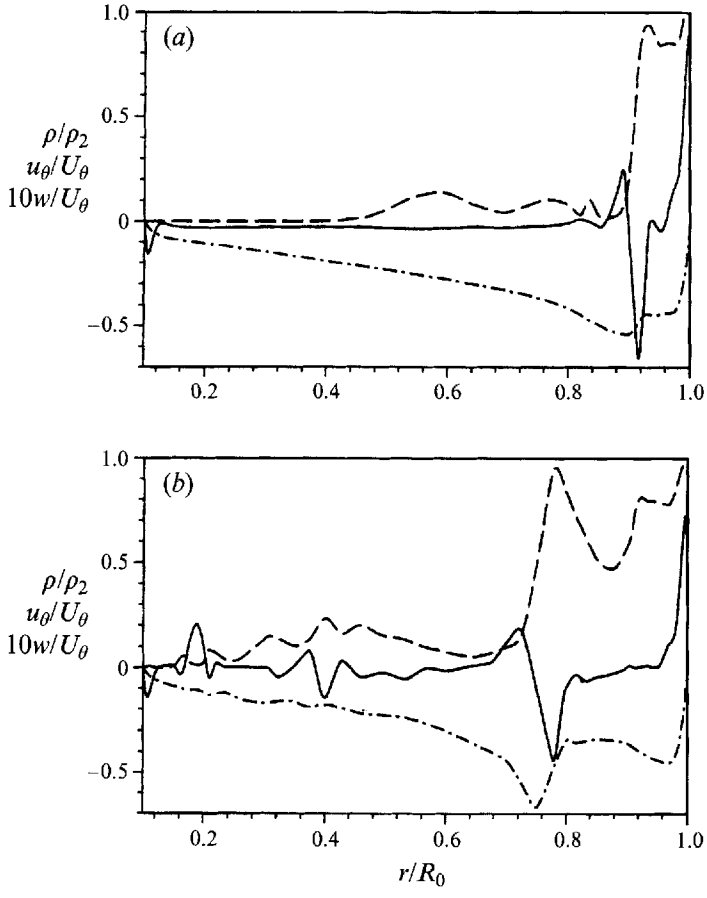

FIGURE 13. Profiles along a horizontal line below the Ekman layer, $\theta/\theta_0 = 0.5$, and $z/H = 0.95$. Lines are: ——, $10w/U_\theta$; — · —, u_θ/U_θ; – – –, ρ/ρ_2, where U_θ is the local lid velocity. (*a*) $t/t_s = 0.9$, (*b*) $t/t_s = 2.0$. (Case SB3D2.)

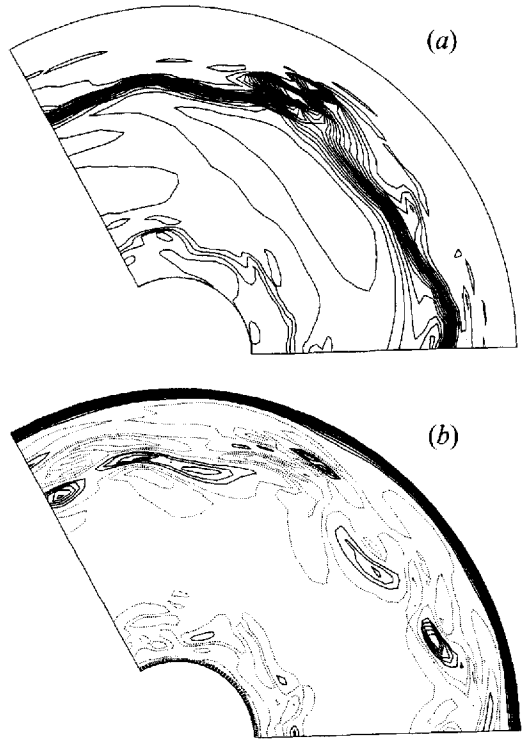

FIGURE 14. Frontal wave structure in a container without the sloping bottom. Contours in a horizontal plane near the top surface, at $z/H = 0.92$ and $t/t_s = 2.0$. (*a*) Density ρ/ρ_2. Contours are from 0 to 1. (*b*) Vertical vorticity $\zeta_r/(U_p/R_0)$. Contours are from -12.5 to 45. (Case FB3D.)

minimum (or its magnitude must have a maximum) near the edge of the upwelling boundary layer which leads to a jet-like structure.

The result in figure 13 is consistent with the argument of O'Brien & Hurlburt in that it shows that the longshore velocity does have a maximum at the edge of the coastal boundary layer. However, the above argument cannot explain why there is another maximum at the surface front. We think that a simple explanation is as follows. The effect of the Coriolis force on an offshore radial velocity is to reduce its longshore velocity in the wind direction. Thus a maximum of the amplitude of the longshore velocity appears at the location where the offshore radial velocity has a minimum. Because the cross-front motion is inhibited, the offshore radial velocity is smallest at the front. It is therefore clear that the longshore velocity should have a maximum at the front location.

In cases where the sloping bottom is replaced with a flat bottom, the frontal waves are not nearly as intensive. Figures 14(*a*) and 14(*b*) show, respectively, the density and vertical vorticity field in a horizontal plane below the Ekman layer for Case FB3D at $t/t_s = 2.0$. The appearance of frontal waves is evident in both the density and vorticity fields. However, the amplitude of the waves is much smaller and the wavelength is larger than that in Case SB3D2 (figure 12). This difference may be explained as follows. First, from table 5, we see that the wavelength L_w scales linearly with the geometric mean of the Rossby radii of deformation of the two layers $\hat{R}$. If the frontal waves appear on a sloping bottom, the depth of the lower layer is smaller than that of a flat bottom. This small depth ratio results in a smaller $\hat{R}$ and, thus, a smaller L_w on a sloping bottom. In addition, a mechanism to generate vorticity waves exists over a

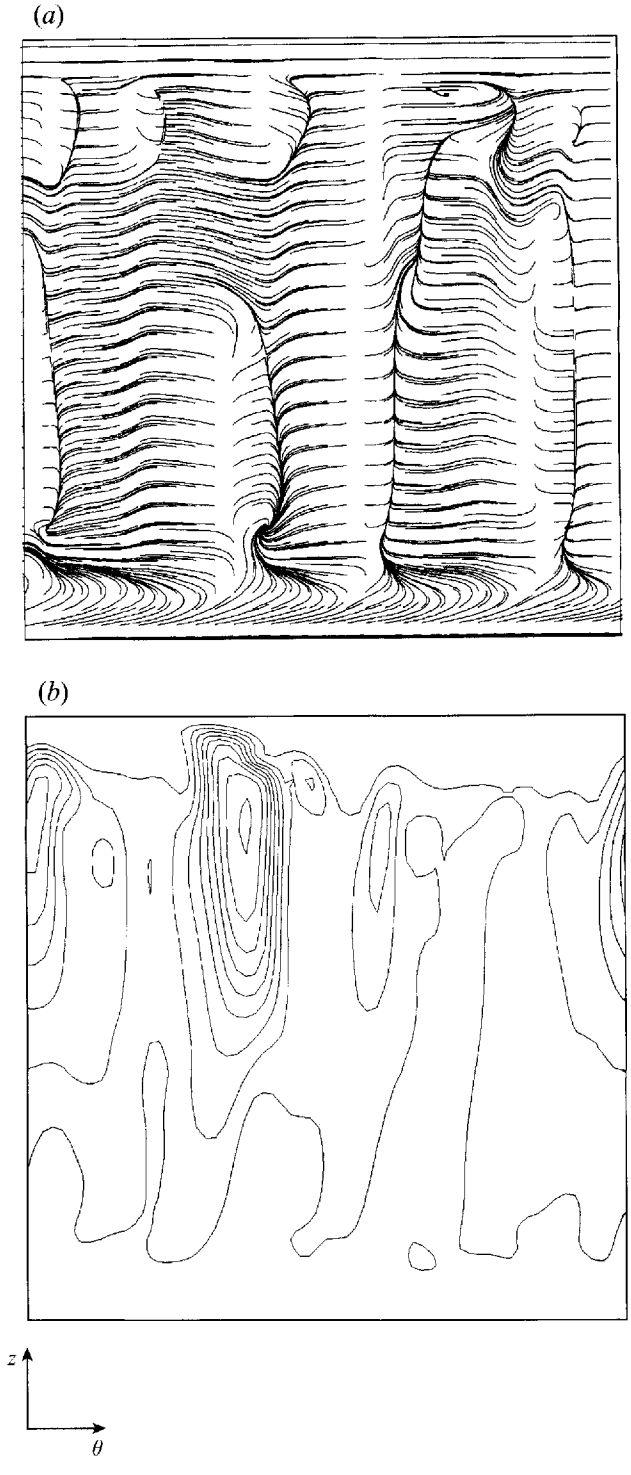

FIGURE 15. (*a*) Streamline pattern and (*b*) density in a longshore plane at $r/R_0 = 0.93$ which cuts through the primary front. The reference frame is travelling with the frontal waves. (Case SB3D2.)

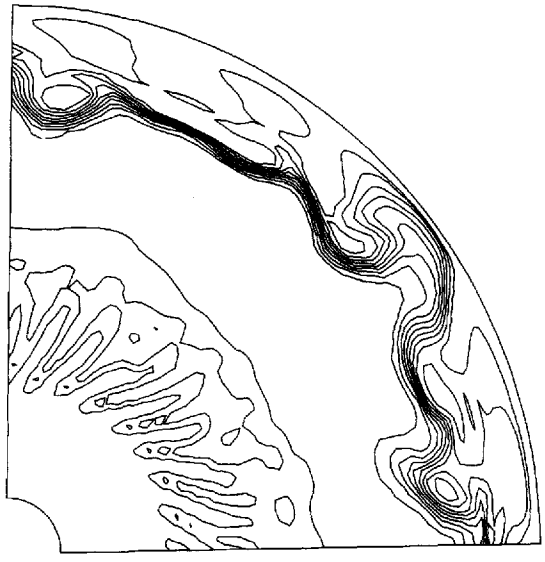

FIGURE 16. Density in a horizontal surface below the top Ekman layer, at $z/H = 0.95$ and $t/t_s = 1.3$. Contours are from 0 to 1. (Case SB3D2.)

sloping bottom. This mechanism has been shown by Longuet-Higgins (1965) (see Gill 1982) to explain the continental shelf waves. The mechanism is, again, based on the conservation of potential vorticity,

$$\frac{\mathrm{d}Q}{\mathrm{d}t} = \frac{\mathrm{d}[(f+\zeta_r)/H_l]}{\mathrm{d}t} = 0. \tag{23}$$

Fluid parcels displaced into deeper water or offshore to larger H_l acquire cyclonic vorticity (positive ζ_r) and fluid parcels displaced into shallower water or onshore to smaller H_l acquire anticyclonic vorticity (negative ζ_r). When small-amplitude azimuthal waves develop at the front, wave crests which have cyclonic vorticity move to deeper water, while wave troughs with anticyclonic vorticity move to shallower water. By the above mechanism, wave crests will acquire more cyclonic vorticity and troughs obtain stronger anticyclonic vorticity. In this way, the waves are amplified.

5.3.3. *Longshore structure*

To reveal the vertical structure of the frontal waves, we plot the streamlines in a longshore plane which cuts through the frontal waves (figure 15*a*). We see that the waves appear in the form of vertical columns. They extend from the bottom of the top Ekman layer to the top of the bottom boundary layer. The local Rossby number of the frontal waves $u_w/f\lambda_w$ is estimated to be about 0.1, which is consistent with the fact that the structure of the waves appears to be predominantly two-dimensional. Figure 15(*b*) shows the density field in the same longshore plane. Being consistent with the velocity field, the fluid appears to be well mixed vertically but displays a structure of two-dimensional columns.

5.3.4. *Collapse of the top inversion layer*

In figure 3(*c*) in which $t/t_s = 0.9$, we see an axisymmetric secondary front which leads the top inversion layer. Later, at $t/t_s = 1.3$ (figure 3*d*), the top inversion layer becomes unstable and splits into azimuthal bands, and still later, at $t/t_s = 2.0$ (figure

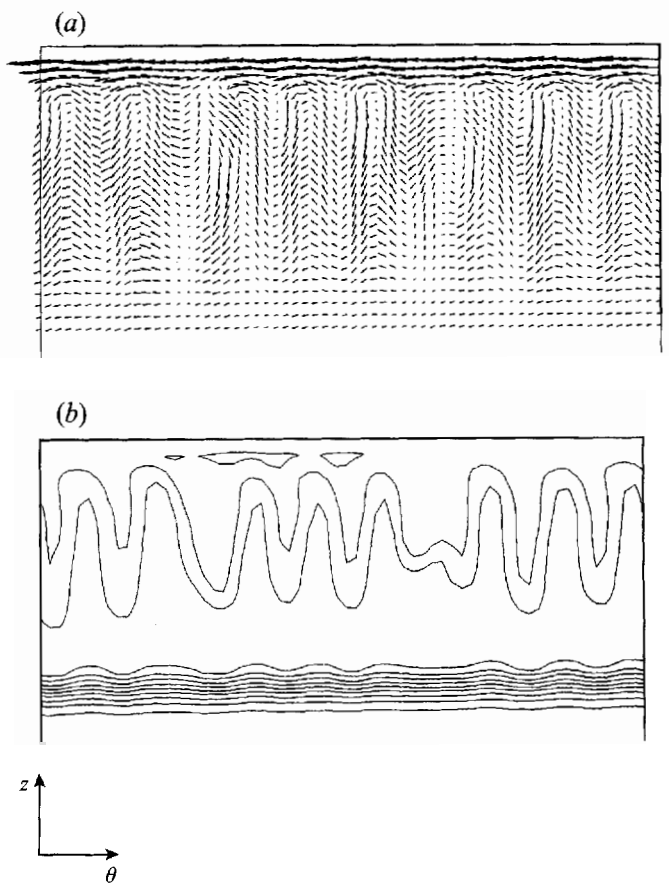

FIGURE 17. (*a*) Velocity vector field and (*b*) density field in a longshore plane at $r/R_0 = 0.46$ and $t/t_s = 1.3$, which cuts through the secondary front. The velocity reference frame is travelling with the waves. (Case SB3D2.)

3*e*), the bands are broken into isolated patches and drop back to the lower layer. The dynamics and structure of this instability are of particular interest.

When the top inversion layer begins to collapse, the azimuthal waves first appear at the secondary front. The waves then propagate toward the outer wall in the form of bands or fingers as interface fluid continues to drop. Figure 16 is the top view of the density field in figure 3(*d*) at $t/t_s = 1.3$. The direction of the bands is at an angle of about 60° to the geostrophic (azimuthal) direction. A total of eight waves are observed in this case which gives an azimuthal wavenumber of 32. Figure 17(*a*) shows the velocity field in a longshore plane cutting through the secondary front. We see that as bands of interface fluid drop, they form columnar vortices in the radial direction. These vortices extend from the edge of the top Ekman layer to the density interface. The density field shown in figure 17(*b*) also displays the columnar structure of the instability.

The bands of interface fluid are further unstable to radial disturbances and break up into isolated patches (Figure 3*e*) which eventually drop back down to the lower layer. Therefore the top inversion layer and the secondary front are not persistent features of the upwelling. They disappear within a couple of spin-up time scales t_s.

It is unclear what the precise dynamics of these instabilities is, and it may involve three-dimensional convective and shear instabilities under the effect of rotation, such

as the Rayleigh–Bénard or the Ekman instability. A detailed stability analysis of these processes is highly desirable but, owing to its complexity, is beyond the scope of the present study.

6. Concluding remarks

LES results confirmed the laboratory experiments of NM87 and some previous field observations. The full Navier–Stokes simulations were able to explicitly reveal the temporal evolution and the spatial structure of the three-dimensional flow field and provide further insight into the upwelling dynamics.

The main results from the simulations of the upwelling on a flat or a sloping bottom are as follows.

(i) The vertical structure of upwelling consists of a persistent primary front, a trailing mixing zone on the shoreside of the front, and a temporary secondary front which leads a top inversion layer.

(ii) A coastal jet is observed. The longshore velocity near the top surface has two maxima, one at the edge of the outer-wall boundary layer, and the other at the location of the front. The frontal jet has a larger longshore velocity.

(iii) The primary front is unstable to azimuthal perturbations and develops large-amplitude baroclinic waves. The wave structure consists of cyclone/anticyclone pairs with associated jet-like motion.

(iv) Wave crests correspond to cyclonic downwelling regions, while wave troughs correspond to anticyclonic upwelling zones.

(v) The frontal waves are much more intensive on a sloping bottom than on a flat bottom with the same maximum water depth.

(vi) The secondary front is unstable to azimuthal perturbations. Its instability, and the associated drop of the top inversion layer, takes the form of radial bands which subsequently break up into isolated patches and eventually sink.

(vii) The flow structures are strongly aligned in the vertical direction, indicating the dominant effect of rotation.

(viii) Reasonable agreement was obtained between the simulation data and past observations, experiments, and theories on upwelling time and length scales such as the surfacing time, the stationary-front width, and the wavelength and wave speed of the frontal waves. Several frontal structures observed in the flow visualizations of NM87, such as the cyclone/anticyclone pairs, plumes, jets and pinched-off cyclones were confirmed.

Several questions remain unanswered. The precise nature of the instability at the secondary front and the collapse of the top inversion layer is unclear. A formal instability analysis of this process is needed and should include the effects of rotation, stratification, three-dimensional shear, and possibly viscosity. More studies of the momentum, velocity and energy balances of the instability process would also be useful.

Simulations of small Ekman number (high Reynolds number) flows in a whole cylinder are highly desirable in order to yield a more direct comparison with experiments. Primitive equation simulations can be made now of field-scale configurations (see, for example, Haidvogel *et al.* 1991 and Song and Haidvogel 1994). The next challenge for the non-hydrostatic LES code presented here is to extend the current simulation to more realistic coastline and shelf geometries, viscosities, density profiles, and spatial and temporal wind variations. This requires an order of magnitude increase in computing power which might be provided by the massively

parallel supercomputers in the near future. An efficient implementation of the current solution method on massively parallel computing systems may be able to bring to reality the detailed simulations and predictions of natural geophysical flows. Towards this end, the code has been ported to the Thinking Machines CM-5 and the sector of an annulus results reported here have been confirmed for the full annulus configuration.

The authors would like to thank Professor J. R. Koseff, Professor J. Ferziger, Professor J. Oliger, Professor T. Maxworthy and Dr S. Narimousa for very helpful discussion. The research was supported by the National Science Foundation through Grant CTS-8719509 and by the Fluid Dynamics Program, Mechanics Division, Office of Naval Research through Grant N-00014-91-J-1200, and computing time on the Cray YMP was provided by the NCAR Scientific Computing Division.

Appendix. The stationary upwelled front width in an annulus

Although derivations for the stationary width of a surface front in a cylinder have been presented by Linden & van Heijst (1984) and Narimousa & Maxworthy (1985), the result for a two-layer stratified flow in an annulus was used here in §5.2. At the stationary state, the radial pressure gradient due to the distortion of the front balances the Coriolis force. Ignoring the effect of turbulent mixing and centrifugal pressure gradient, and assuming that the upper layer is spun-up to the plate velocity, we have

$$-fr\Delta\Omega = g'\frac{\mathrm{d}\eta_s}{\mathrm{d}r}, \tag{A 1}$$

where $r\Delta\Omega$ is the plate velocity, $f = 2\Omega$ is the Coriolis parameter, r is the radial coordinate from the rotation axis, g' is the reduced gravity and η_s is the depth of the front from the surface. Integrating (A 1), we obtain

$$-\frac{f\Delta\Omega r^2}{2g'} = \eta_s + c, \tag{A 2}$$

where c is the integration constant. If R is the distance from the surface front to the rotation axis, then, at $r = R, \eta_s = 0$. Substituting this boundary condition into (A 2), we have

$$\eta_s = \frac{f\Delta\Omega}{2g'}(R^2 - r^2). \tag{A 3}$$

Conservation of volume of the upper layer in an annulus requires that

$$2\pi\int_{R_1}^{R}\eta_s r\,\mathrm{d}r = \pi h_0[R_0^2 - R_1^2], \tag{A 4}$$

where h_0 is the initial depth of the upper layer and R_0 and R_1 are, respectively, the radii of the outer and inner walls. Substituting (A 3) into (A 4) and solving for R, we obtain

$$R = \left\{R_1^2 + \left[\frac{4g'h_0(R_0^2 - R_1^2)}{f\Delta\Omega}\right]^{1/2}\right\}^{1/2}. \tag{A 5}$$

The stationary front width λ_s is

$$\lambda_s = R_0 - R. \tag{A 6}$$

REFERENCES

ALLEN, J. S. 1972*a* Upwelling of a stratified fluid in a rotating annulus: steady state. Part 1. Linear theory. *J. Fluid Mech.* **56**, 429–445.

ALLEN, J. S. 1972*b* Upwelling of a stratified fluid in a rotating annulus: steady state. Part 2. Numerical solutions. *J. Fluid Mech.* **59**, 337–368.

ALLEN, J. S. 1973 Upwelling and coastal jets in a continuously stratified ocean. *J. Phys. Oceanogr.* **3**, 245–257.

CALDWELL, D. R., VAN ATTA, C. W. & HELLAND, K. N. 1972 A laboratory study of the turbulent Ekman layer. *Geophys. Fluid Dyn.* **3**, 125–160.

CHARNEY, J. G. 1955 The generation of oceanic currents by wind. *J. Mar. Res.* **14**, 477–498.

CHIA, F. R., GRIFFITHS, R. W. & LINDEN, P. F. 1982 Laboratory experiments on fronts. Part II. The formation of cyclonic eddies at upwelling fronts. *Geophys. Astrophys. Fluid Dyn.* **19**, 189–206.

COLIN, C. 1988 Coastal upwelling events in front of the Ivory Coast during the FOCAL program. *Oceanologica ACTA* **11**, 125–137.

EADY, E. T. 1949 Long waves and cyclone waves. *Tellus* **1**, 35–52.

EKMAN, V. M. 1905 *Ark. Mat. Astr. Fys.* **2** (11), 1–52.

GARVINE, R. W. 1971 A simple model of coastal upwelling dynamics. *J. Phys. Oceanogr.* **1**, 169–179.

GERMANO, M., PIOMELLI, U., MOIN, P. & CABOT, W. H. 1991 A dynamic subgrid-scale eddy viscosity model. *Phys. Fluids* A **3**, 1760–1765.

GILL, A. E. 1982 *Atmosphere-Ocean Dynamics.* Academic Press.

GREENSPAN, H. P. 1968 *The Theory of Rotating Fluids.* Cambridge University Press.

GRIFFITHS, R. W. & LINDEN, P. F. 1981 The stability of buoyancy driven coastal currents. *Dyn. Atmos. Oceans* **5**, 281–306.

GRIFFITHS, R. W. & LINDEN, P. F. 1982 Laboratory experiments on fronts. Part I. Density driven boundary currents. *Geophys. Astrophys. Fluid Dyn.* **19**, 159–187.

HAIDVOGELN, D. B., BECKMAN, A. & HEDSTROM, K. S. 1991 Dynamical simulations of filament formation and evolution in the coastal transition zone. *J. Geophys. Res.* **96**, 15017–15040.

HALPERN, D. 1976 Structure of a coastal upwelling event observed off Oregon during July 1973. *Deep-Sea Res.* **23**, 495–508.

HART, J. E. 1980 An experimental study of nonlinear baroclinic instability and mode selection in a large basin. *Dyn. Atmos. Oceans* **4**, 115–135.

HIDAKA, K. 1954 A contribution to the theory of upwelling and coastal currents. *Trans. Am. Geophys. Union* **35**, 431–444.

HIDE, R. 1971 Laboratory experiments of free thermal convection in a rotating fluid subject to a horizontal temperature gradient and their relation to the theory of the global atmospheric circulation. In *The Global Circulation of the Atmosphere*, pp. 196–221. R. Met. Soc. and Am. Met. Soc.

HSUEH, Y. & KENNEY, R. N. 1972 Steady coastal upwelling in a continuously stratified ocean. *J. Phys. Oceanogr.* **2**, 27–33.

HURLBURT, H. E. & THOMPSON, J. D. 1973 Coastal upwelling on a β plane. *J. Phys. Oceanogr.* **3**, 16–32.

HUYER, A., SMITH, R. L. & PALUSZKIEWICZ, T. 1987 Coastal upwelling off Peru during normal and El Nino times, 1981–1984. *J. Geophys. Res.* **92**, 14297–14307.

IKEDA, M., MYSAK, L. A. & EMERY, W. J. 1984 Observation and modelling of satellite-sensed meanders and eddies off Vancouver Island. *J. Phys. Oceanogr.* **14**, 3–21.

KILLWORTH, P. D., PALDOR, N. & STERN, M. 1984 Wave propagation and growth on a surface front in a two-layer geostrophic current. *J. Mar. Res.* **42**, 761–785.

LINDEN, P. F. & HEIJST, G. J. F. VAN 1984 Two-layer spin up and frontogenesis. *J. Fluid Mech.* **143**, 69–94.

LONGUET-HIGGINS, M. S. 1965 On group velocity and energy flux in planetary wave motions. *Deep-Sea Res.* **11**, 35–43.

MONISMITH, S. G. 1986 An experimental study of the upwelling response of stratified reservoirs to surface shear stress. *J. Fluid Mech.* **171**, 407–439.

MOOERS, C. N. K., COLLINS, C. A. & SMITH, R. L. 1976 The dynamics structure of the frontal zone in the coastal upwelling region off Oregon. *J. Phys. Oceanogr.* **6**, 3–21.

MOOERS, C. N. K. & ROBINSON, A. R. 1984 Turbulent jets and eddies in the California current and inferred cross-shore transport. *Science* **223**, 51–53.

NARIMOUSA, S. & MAXWORTHY, T. 1985 Two-layer model of shear-driven coastal upwelling in the presence of bottom topography. *J. Fluid Mech.* **159**, 503–531.

NARIMOUSA, S. & MAXWORTHY, T. 1987 Coastal upwelling on a sloping bottom: the formation of plumes, jets and pinched-off cyclones. *J. Fluid Mech.* **176**, 169–190 (referred to herein as NM87).

NARIMOUSA, S., MAXWORTHY, T. & SPEDDING, G. R. 1991 Experiments on the structure and dynamics of forced, quasi-two-dimensional turbulence. *J. Fluid Mech.* **223**, 113–133.

O'BRIEN, J. J. & HURLBURT, H. E. 1972 A numerical model of coastal upwelling. *J. Phys. Oceanogr.* **2**, 14–26.

PEDLOSKY, J. 1974 Longshore currents, upwelling and bottom topography. *J. Phys. Oceanogr.* **4**, 214–226.

PEFFLEY, M. B. & O'BRIEN, J. J. 1976 A three-dimensional simulation of coastal upwelling off Oregon. *J. Phys. Oceanogr.* **6**, 164–180.

PELEGRI, J. L. & RICHMAN, J. G. 1993 On the role of shear mixing during transient coastal upwelling. *Continental Shelf Res.* **13**, 1363–1400.

PETRIE, B., TOPLISS, B. J. & WRIGHT, D. G. 1987 Coastal upwelling and eddy development off Nova Scotia. *J. Geophys. Res.* **92**, 12979–12991.

PHILLIPS, N. A. 1954 Energy transformations and meridional circulations associated with simple baroclinic waves in a two-level, quasi-geostrophic model. *Tellus* **6**, 273–286.

PRELLER, R. & O'BRIEN, J. J. 1980 The influence of bottom topography on upwelling off Peru. *J. Phys. Oceanogr.* **10**, 1377–1398.

RIENECKER, M. M. & MOOERS, C. N. K. 1987 Dynamical interpolation and forecast of the evolution of mesoscale features off Northern California. *J. Phys. Oceanogr.* **17**, 1189–1213.

ROUGHGARDEN, J., GINES, S. & POSSINGHAM, H. 1988 Recruitment dynamics in complex life cycles. *Science* **241**, 1460–1466.

RYTHER, J. H. 1969 Photosynthesis and fish production in the sea. *Science* **166**, 72–76.

SANDERS, P. M. 1973 The instability of a baroclinic vortex. *J. Phys. Oceanogr.* **3**, 61–65.

SMAGORINSKY, J. 1963 General circulation experiments with the primitive equations, I. The basic experiment. *Mon. Weath. Rev.* **91**, 99–164.

SMITH, R. L. 1968 Upwelling. *Oceanogr. Mar. Biol. Ann. Rev.* Allen **6**, 11–47.

SMITH, R. L. 1978 Poleward propagating perturbations in currents and sea level along the Peru coast. *J. Geophys. Res.* **83**, 6083–6092.

SMITH, R. L., MOOERS, C. N. K. & ENFIELD, D. B. 1971 Mesoscale studies of the physical oceanography in two coastal upwelling regions: Oregon and Peru. In *Fertility of the Sea* vol. 2, pp. 513–535. Gordon and Breach.

SONG, Y. & HAIDVOGEL, D. 1994 A semi-implicit ocean circulation model using a generalized topography-following coordinate system. *J. Comput. Phys.* **115**, 228–244.

SVERDRUP, H. U. 1938 On the processes of upwelling. *J. Mar. Res.* **1**, 155–164.

YOSHIDA, K. 1955 Coastal upwelling off the California coast. *Rec. Oceanogr. Works Japan* **2** (2), 1–13.

YOSHIDA, K. 1967 Circulation in the eastern tropical oceans with special reference to upwelling and undercurrents. *Japan J. Geophys.* **4** (2), 1–75.

ZANG, Y. 1993 On the development of tools for the simulation of geophysical flows. PhD dissertation, Dept. Mech. Engng, Stanford University.

ZANG, Y., STREET, R. L. & KOSEFF, J. R. 1993*a* Large eddy simulation of turbulent cavity flow using a dynamic subgrid-scale model. In *Engineering Applications of Large Eddy Simulations* (ed. S. A. Ragab & U. Piomelli). ASME FED vol. **162**, pp. 121–126.

ZANG, Y., STREET, R. L. & KOSEFF, J. R. 1993*b* A dynamic mixed subgrid-scale model and its application to turbulent recirculating flows. *Phys. Fluids* A **5**, 3186–3196.

ZANG, Y., STREET, R. L. & KOSEFF, J. R. 1994 A non-staggered grid, fractional step method for time-dependent incompressible Navier–Stokes equations in curvilinear coordinates. *J. Comput. Phys.* **114**, 18–33.